Highly Efficient 2D Materials Engineered Perovskite/Si Tandem Bifacial Cells Beyond 29%

Antonio Agresti, Sara Pescetelli, Erica Magliano, Giuseppe Bengasi, Carmelo Connelli, Cosimo Gerardi, Hanna Pazniak, Francesco Bonaccorso, Marina Foti, Aldo Di Carlo

Highly Efficient 2D Materials Engineered Perovskite/Si Tandem Bifacial Cells Beyond 29%

Antonio Agresti, Sara Pescetelli, Erica Magliano, Giuseppe Bengasi, Carmelo Connelli, Cosimo Gerardi, Hanna Pazniak, Francesco Bonaccorso, Marina Foti, and Aldo Di Carlo

***Abstract*—Perovskite/Silicon tandem technology represents a promising route to achieve 30% power conversion efficiency (PCE), by ensuring low levelized costs energy. In this article, we develop a mechanically stacked 2T perovskite/silicon tandem solar cell, with subcells independently fabricated, optimized, and subsequently coupled by contacting the back electrode of the mesoscopic perovskite top cell with the texturized and metalized front contact of the silicon bottom cell. The possibility to separately optimize the two sub-cells allows to carefully choose the most promising device structure for both top and bottom cells. Indeed, semitransparent perovskite top cell performance is boosted through the use of selected two-dimensional materials to tune the device interfaces. In addition, a protective buffer layer is used to prevent damages induced by the transparent electrode sputtering deposition over the hole transporting layer. A textured amorphous/crystalline silicon heterojunction cell fabricated with a fully industrial in-line production process is here used as state of art bottom cell. The perovskite/c-Si tandem device demonstrates remarkable PCE of 28.7%. Moreover, we demonstrate the use of a bifacial silicon bottom cell, as a viable way for overcoming the current matching constrain imposed by the 2T configuration. Here, the current generation difference between perovskite and c-Si cells is compensated by exploiting the albedo radiation thanks to the bifaciality of the commercial c-Si cell used in this article. Considering standard rear irradiation, final power generation density above 32 mW/cm^2 can be achieved, paving the way for a tandem technology customable according to the final installation site.**

***Index Terms*—Albedo radiation, bifaciality, perovskite/silicon tandem solar cells, photovoltaics (PVs), two-dimensional (2-D) materials, two-terminal (2T) mechanically stacked architecture.**

Manuscript received 1 June 2022; revised 5 August 2022; accepted 8 October 2022. Date of publication 25 October 2022; date of current version 28 November 2022. This work was supported in part by the European Union's Horizon 2020 research and innovation programme under Grant GrapheneCore3 N° 881603. *(Corresponding authors: Antonio Agresti; Sara Pescetelli; Aldo Di Carlo.)*

Antonio Agresti, Sara Pescetelli, and Erica Magliano are with the Center for Hybrid and Organic Solar Energy, Electronic Engineerng Department, University of Rome Tor Vergata, 00133 Rome, Italy (e-mail: antonio.agresti@uniroma2.it; pescetel@uniroma2.it; erica.magliano@uniroma2.it).

Giuseppe Bengasi, Carmelo Connelli, Cosimo Gerardi, and Marina Foti are with the Enel Green Power SpA, Contrada Blocco Torrazze, 95121 Catania, Italy (e-mail: giuseppe.bengasi@enel.com; carmelo.connelli@enel.com; cosimo.gerardi@enel.com; marina.foti@enel.com).

Hanna Pazniak is with the CNRS, Grenoble INP, LMGP, Université Grenoble Alpes, F-38000 Grenoble, France (e-mail: poznyak.a87@gmail.com).

Francesco Bonaccorso is with the BeDimensional, 16163 Genova, Italy (e-mail: francesco.bonaccorso@iit.it).

Aldo Di Carlo is with the Istituto di Struttura della Materia (CNR-ISM) National Research Council, 00133 Rome, Italy, and also with C.H.O.S.E. (Center for Hybrid and Organic Solar Energy), Electronic Engineerng Department, University of Rome Tor Vergata, 00133 Rome, Italy (e-mail: aldo.dicarlo@uniroma2.it).

Color versions of one or more figures in this article are available at https://doi.org/10.1109/JPHOTOV.2022.3214345.

Digital Object Identifier 10.1109/JPHOTOV.2022.3214345

I. Introduction

THE emerging perovskite technology demonstrated power conversion efficiency (PCE) overcoming 25% by employing cost effective solution-based manufacturing processes. [1] The exceptional physical properties such as long charge diffusion length (up to 1 μm), broad absorption spectrum in the visible range and bipolar charge transport make perovskite-based photovoltaics (PVs) promising for industrial exploitations [2], [3] as well as for space applications. [4] Moreover, efficient and stable devices can be produced by employing scalable and low-cost printing techniques, easily embedded in roll-to-roll or sheet-to-sheet production lines. [5] Indeed, the impressive potentiality of perovskite technology has been already demonstrated to compete on equal footing with traditional inorganic PV or to work in synergy with established silicon technology in tandem cell configuration. [6] As a matter of fact, the energy bandgap (E_{BG}) of perovskite materials can be finely tuned by compositional engineering, to meet the absorption properties required by each specific tandem architecture. This offers a great advantage to use perovskite-based device in different tandem designs such as the wide E_{BG} top cell or low E_{BG} bottom cell [7]. Moreover, with the high optoelectronic quality of the perovskite bulk, the main recombination losses occur at the interfaces with the charge selective layers, that can be altered by utilizing interlayers, [8] surface modifications, [9] or proper contact materials [10]. Thus, perovskite-based tandem solar cells can potentially reach PCEs over 30%, as long as the device is carefully designed for guaranteeing optimal optical and electrical coupling among the composing sub-cells, in turn optimized in term of electrical performance [11]. Among the demonstrated perovskite-based tandem devices, those involving crystalline silicon (c-Si) cells received by far the highest attention since c-Si cells are currently the leading technology in the global PV market, representing 95% of the total production [12].

In this regards, both two-terminal (2T) and four-terminal (4T) perovskite/silicon tandem solar cells have been recently reported to reach PCEs beyond record c-Si cells, [13], [14] with a certified record efficiency of 31.3% from EPFL/CSEM research centers [15]. Al-Ashouri et al. [16] demonstrated a record monolithic perovskite/silicon tandem with a certified PCE of 29.15%. The impressive PCE and stability (in air, without encapsulation, retaining 95% of its initial efficiency after 300 h of operation) was made possible by the use of a self-assembled, methyl-substituted carbazole monolayer (SAM) as hole-selective layer in the perovskite top cell. The SAM

provided both fast extraction and efficient passivation at the hole-selective interface while slowing down the light-induced halide segregation of the tandem-relevant perovskite composition employed ($Cs_{0.05}(FA_{0.77}MA_{0.23})_{0.95}Pb(I_{0.77}Br_{0.23})_3$) owing a E_{BG} of 1.68 eV. This article clearly identified the interface optimization of the perovskite top cell as the key point to boost the tandem device performance and stability over the current state of the art. As a further advantage, the 2T monolithic structure with a direct series connection between the two sub-cells requires only two external electrodes. This yields final costs similar to single-junction modules, which is highly desirable to reach low levelized costs of energy (LCOE) [17]. Despite that, several fabrication constrains should to be taken into account when speaking about a monolithic 2T architecture. For example, mesoscopic perovskite solar cells (PSCs) require a high-temperature ($T > 400$ °C) process not compatible with the state-of-the-art heterojunction (HJT) c-Si solar cells, withstanding temperatures lower than 200 °C [18]. Moreover, the textured front side of Si HJT cells, as optimized for infrared light trapping and primary reflection reduction, hinders an easy solution processing of the perovskite top cell. In fact, the typical texturing process of HJT solar cells, generates random pyramids with a height of several microns. The conformal deposition via solution processes of the PSC layers on the texturized surface becomes very critical and requires the use of thicker perovskites, modified texturing to reduce the pyramid height and additives to enhance the charge diffusion length [18], [19], [20], [21]. To overcome such limitations, we recently proposed a mechanically stacked 2T perovskite/silicon tandem solar cell, with the subcells independently fabricated, optimized, and subsequently coupled by contacting the back transparent electrode of the mesoscopic perovskite top cell with the texturized and metalized front contact of the silicon bottom cell [22]. The simple, yet integrated, electrical connection between the perovskite cell and the silicon cell permits to avoid the use of the recombination layer which typically represents one of the critical optimization aspects of the monolithic tandem cell [23].

However, even in 2T mechanically stacked configuration, the current matching condition still force the design of perovskite top cell, imposing an ideal E_{BG} of the perovskite absorber around 1.7 eV [24].

Despite perovskite E_{BG} can be enlarged by replacing iodine with bromine, the photo-induced segregation, [7] thermal degradation, [25] and mechanical instabilities [26] limit the performance of the as-obtained tandem devices. Indeed, when the bromide composition exceeds about 20% of the halides, the material reversibly segregates into an iodide-rich phase and a bromide-rich phase under illumination, causing: reduced V_{OC} due to increased thermalization losses in the absorber; current collection inhibition due to carrier accumulation in the smaller bandgap (I-rich) phase, eventually leading to a current mismatching between the two cells of the 2T tandem device. [27] As alternative strategy for 2T architectures where current matching is required, consists in shifting the top-cell E_{BG} to lower values compared to the optimal one and increasing the current generation of the bottom cell. This can be achieved by using a bifacial c-Si bottom cell that can benefits from the absorbance of the "albedo" radiation on the cell rear side. The "albedo" is defined as the measure of the reflected and scattered light from the surroundings, out of the total solar radiation. In PV devices with the transparent rear side, such albedo radiation can contribute to power generation, by inducing a linear increase of the generated device current with the albedo increase. The use of the albedo radiation for 4T perovskite/Si tandem have been recently demonstrated as an effective way to achieve conversion efficiency exceeding 30%, which is higher than those of both the top and bottom subcells. [28] Notably, this efficiency is also greater than the Schockley–Quiesser limit of the c-Si solar cell (approximately 29.43%).

In particular, theoretical studies considering flat albedos have reported a significant red shift (from 1.71 eV to the range 1.60–1.65 eV) in optimal top-cell E_{BG} with increasing albedo. [28], [29] In addition, De Bastiani et al. [30] recently demonstrated that bifacial monolithic 2T perovskite/silicon tandem solar cells exploiting albedo radiation achieved certified PCE >25% under monofacial AM1.5G 1 sun illumination, while reaching generated power densities (GPD) as high as ∼26 mW cm^{-2} under outdoor testing. The authors investigated the perovskite E_{BG} required to attain optimized current matching under a variety of realistic illumination and albedo conditions. As main results, the bifacial tandem employing a perovskite top cell with a 1.62 eV E_{BG} generates a slightly lower current (∼0.5 mA cm^{-2}) in monofacial operation mode, when compared with an opaque metal rear electrode and a perovskite E_{BG} of 1.68 eV. However, in the presence of a 20 mW cm^{-2} albedo irradiance, the 1.62 eV band-gap perovskite cell employed in tandem configuration clearly surpasses its monofacial counterparts.

In this article, we report the optimization of a semi-transparent perovskite top cell with E_{BG} 1.62 eV and its use in bifacial perovskite/c-Si tandem devices when mechanically coupled with a standard commercial bifacial c-Si HJT bottom cell, provided by the major PV Italian producer, Enel green power (EGP). While the insertion of a protective buffer layer (PBL) allowed to avoid undesirable fill factor (FF) drop in the perovskite top cell *I–V* curve, the use of specifically selected bi-dimensional (2-D) materials [31] allowed to achieve top PCE of 28.7% in tandem devices. Moreover, testing the as-optimized tandem cell in presence of a variable albedo radiation, the device current increases, linearly filling the J_{SC} gap between top and bottom cells. We recorded a GPD above 29 mW/cm^2 while predicting the possibility to reach a GPD up to 32 mW/cm^2.

II. Results and Discussion

A. Optimization of Semitransparent Perovskite Top Cell: The Role of the Protective Buffer Layer

The reference structure used for the semi-transparent perovskite top cell ([see Fig. 1(a)] is glass-FTO/cTiO$_2$/mTiO$_2$/perovskite/poly(triarylamine)-PTAA/ITO transparent electrode. As first step, semitransparent perovskite top cell was optimized in term of electrical performance by improving the hole selective contact. Indeed, when semitransparent ITO is deposited by mean of sputtering deposition technique, damages can be induced over PTAA HTL

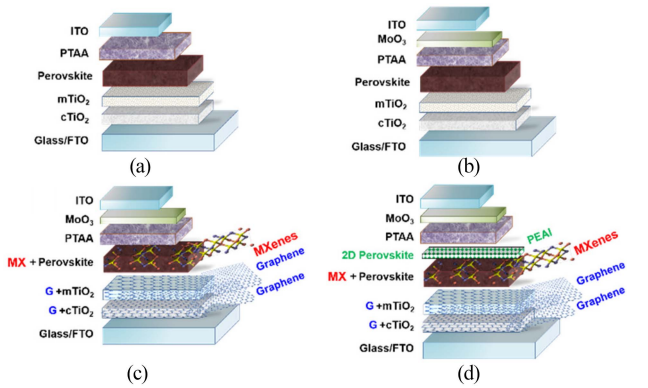

Fig. 1. Tested device structures for perovskite top cell. (a) Semitransparent device with PTAA/ITO electrode. (b) Semitransparent device with optimized PTAA/MoO_3/ITO electrode, named ref. in the main text. (c) Semitransparent device with optimized PTAA/MoO_3/ITO electrode, graphene into the ETL and MXenes into the perovskite absorber, named G/MX in the main text. d) fully 2-D-material engineered semi-transparent device with optimized PTAA/MoO_3/ITO electrode, named G/MX/PEAI in the main text.

TABLE I
ELECTRICAL PARAMETERS FOR THE TESTED PEROVSKITE TOP CELL STRUCTURES EXTRACTED BY *J–V* CHARACTERISTICS REPORTED IN FIG. 2

MoO_3 thickness (nm)	*PCE (%)*	*AIT (%)*
0	7.03	76.5
2	12.5	75.4
3.5	15.4	75.2
5	14.8	73.1
10	13.9	71.2

[32]. Thus, the as-realized PTAA/ITO interface suffers from reduced capability in transferring and collecting hole carriers by slowing down the charge dynamic and increasing the PSC series resistance.

This is clearly identified in the evident S-shaped current–voltage (*I–V*) characteristic of semi-transparent device when compared with the opaque one [32]. The S-shape stems from a reduced shunt resistance (R_{SH}) and an increased series resistance (R_S) strongly penalizing the device FF, reduced of about 30% (PCE reduced of about 50%) when compared with the opaque reference cells.

Instead of the use of more robust transporting materials (HTMs) to replace PTAA, an alternative way to prevent damages of the PTAA layer during ITO sputtering deposition consists in a thin MoO_3 layer deposited by high-vacuum thermal evaporation as PBL. The PBL thickness (3.5 nm) was optimized in term of transparency over the absorption wavelength range of Si cell, as well as in term of the final device performance, taking care about the charge extracting capability at the PTAA/MoO_3/ITO electrode.

Table I gives the top cell PCE while Table II resumes its averaged infrared transmittance (AIT) in the range from 800 to 1200 nm by varying the MoO_3 thickness. Since 3.5 nm results in the optimal tradeoff among cell PCE and AVT, we selected such MoO_3 thickness for the following optimizations of the perovskite top cell.

TABLE II
PCE AND AIT IN THE 800–1200 NM RANGE OF THE PEROVSKITE TOP CELL BY VARYING THE MoO_3 THICKNESS

Device	*V_{OC} (V)*	*J_{SC} (mA/cm²)*	*FF (%)*	*PCE (%)*
ITO	0.92	19.77	38.46	7.03
PBL/ITO (ref.)	0.99	20.97	74.07	15.39

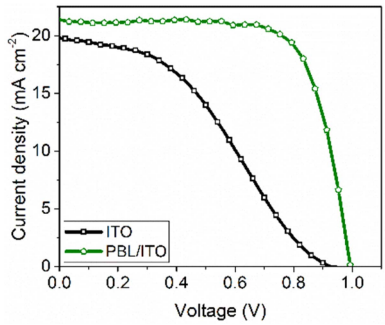

Fig. 2. *J–V* characteristics for different perovskite top cells structures: Black curve for ITO electrode [see Fig. 1(a)], green curve for PBL-modified ITO electrode [see Fig. 1(b)] named ref. in the main text. *I–V* characteristics are acquired under 1 sun irradiation; device active area 0.09 cm^2.

TABLE III
ELECTRICAL PARAMETERS FOR THE TESTED PEROVSKITE/C-SI TANDEM CELL STRUCTURES, EXTRACTED BY *J–V* CHARACTERISTICS REPORTED IN FIG. 4

Device	*V_{OC} (V)*	*J_{SC}(mA/cm²)*	*FF(%)*	*PCE(%) or GPD (mW/cm²)*
Ref. (FS)	1.77	18.82	74.96	24.97
Ref. (RS)	1.78	18.834	78.75	**26.4**
G/MX/PEAI (FS) No albedo	1.82	19.02	79.33	27.53
G/MX/PEAI (RS) No albedo	1.84	19.01	81.64	**28.69**
G/MX/PEAI (FS) albedo (2.4 mW/cm²)	1.83	19.4	78.64	27.98
G/MX/PEAI (RS) albedo (2.4 mW/cm²)	1.83	19.56	81.51	**29.13**

The *I–V* curves for champion semi-transparent perovskite cell employing the optimized PBL is reported in Fig. 2. The insertion of a PBL prevented the S-shape in the device *I–V* curve by restoring the device FF and PCE, finally overcoming 74% and 15% respectively (the main electrical parameters for the semi-transparent devices are reported in Table I).

B. Optimization of the 2T Mechanically Stacked Perovskite/Si Tandem Devices: The Role of 2-D Materials

The as-optimized perovskite top cell with the following structure FTO/$cTiO_2$/$mTiO_2$/perovskite/PTAA/MoO_3/ITO was used in combination with a commercial bifacial c-Si HJT cell in tandem configuration and named as "ref." in the following

TABLE IV
ELECTRICAL PARAMETERS FOR THE BEST TESTED TANDEM DEVICES EXTRACTED BY *J–V* CHARACTERISTICS REPORTED IN FIG. 5

Device	V_{OC} *(V)*	J_{SC}*(mA/cm²)*	*FF(%)*	*PCE(%)*
Ref.	1.78	18.78	78.8	26.4
G/MX	1.78	19.05	79.7	27.1
G/MX/PEAI	1.84	19.10	81.6	28.7

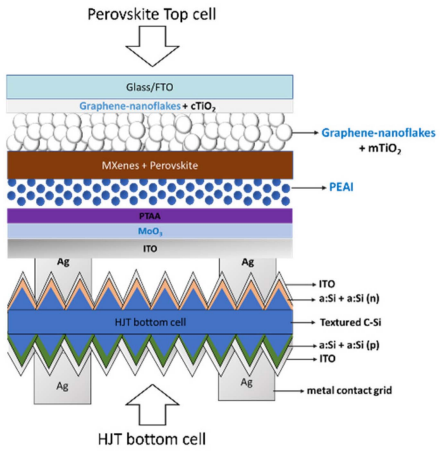

Fig. 3. Schematic representation of 2T mechanically stacked perovskite/Si tandem device. The blue color underlines the engineering strategies employed for perovskite top cell based on the use of 2-D materials and the insertion of a PBL, as schematically reported in Fig. 1(d).

of the manuscript. The bottom cell was prepared within EGP industrial solar cell factory, in standard industrial production condition and without further optimization, including a standard texturing of the HJT cell. In particular, the Si-cell (active area 0.54 cm^2) was mechanically coupled with the perovskite top cell by applying a proper pressure over the contact area between the two sub-cells, through a specifically designed sample holder (no transparent conductive adhesive applied among the subcells). A schematic view of the mechanical coupling between the two cells is reported in Fig. 3.

It is worth to note that the best-efficient tandem device showed a PCE of 26.4% (Table III) overcoming our recently published results, [22] thanks to the optimization of perovskite device structure in term of device layer thickness ($mTiO_2$ thickness was reduced by adjusting the TiO_2 paste composition, see materials and methods section for further details), perovskite composition (for further details, refers to the methods section), and the use of the PBL (forward and reverse scan *I–V* curves are reported in Fig. 4(a) for the best performing tandem ref. cell).

With the aim to further improve the tandem device performance, we further explored the use of interface engineering based on 2-D materials for tuning the perovskite/charge transporting layer (CTL) interface properties [31]. Indeed, considering the typical sandwich structure of the perovskite top cell, interfacial vacancies, defects and energy barriers can dramatically affect the device performance while charges trapped at the interface can trigger the device degradation [33]. This highlights the importance of a proper device design in terms of energy level alignment and the possibility to tune somehow the optoelectronic properties of constituting layers. Energy levels in

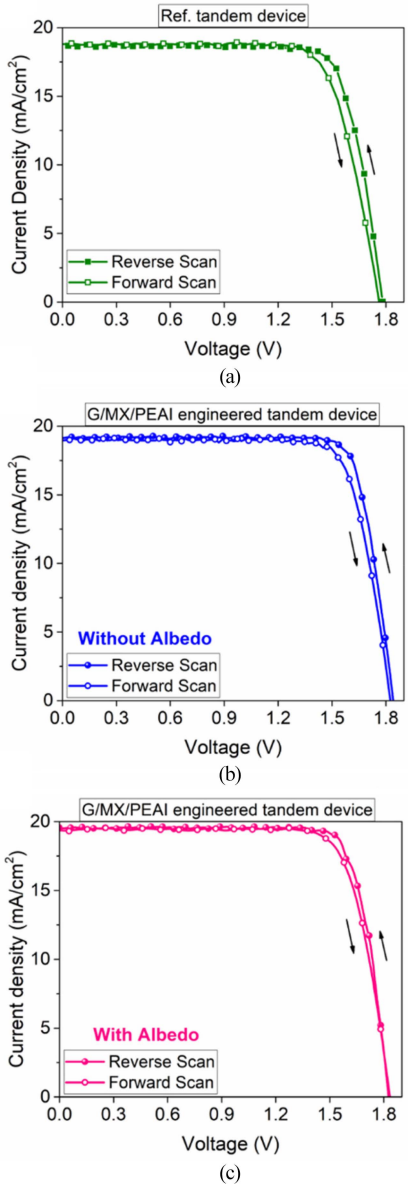

Fig. 4. *J–V* characteristics cosidering both forward and reverse voltage scans for (a) Ref. perovskite/c-Si tandem device employing perovskite top cell enginerred with the PBL, as schematized in Fig. 1(b). (b) and (c) Perovskite/c-Si tandem device employing perovskite top cell enginerred with PBL and the use of 2-D materials into the cell structure (named G/MX/PEAI), as schematized in Fig. 1(d). Curves in panel (b) Were acquired without employing any rear irradiation while curves in panel (c) Considering an albedo radiation of 2.4 mW/cm^2 (see materials and methods sections for further details). *I–V* characteristics are acquired under 1 SUN irradiation; device active area 0.54 cm^2.

halide perovskite semiconductors and materials for CTLs cannot be simply controlled by chemical doping as for Si and *III–V* semiconductors.

Thus, the use of interface engineering based on 2-D materials considered in this article represents a winning strategy for trap passivation at perovskite/CTL interfaces and energy level alignment, leading to an overall enhancement of the perovskite top cell performance and eventually to the perovskite/c-Si tandem device PCE. By exploiting the approach of interface engineering based on 2-D materials, already successfully demonstrated in our previous works, [34], [35], [36], we further optimized the

perovskite top cell structure by implementing the following detailed engineering strategies.

Regarding the ETL, the addition of graphene nanoflakes (G-nfs) into the mesoporous TiO_2 ($mTiO_2$) ETL resulted in very good crystalline quality of the perovskite small crystals wrapped into $mTiO_2$, with a trap density about one order of magnitude lower than that found for pristine ETL [37].

The use of the as-modified G-nfs/ETL resulted in a stability improvement of $mTiO_2$/perovskite interface under real working conditions, as demonstrated by X-ray photoelectron spectroscopy depth profile analysis, time-of-flight secondary ion mass spectrometry (ToF-SIMS) 3-D imaging [38] and femtosecond transient absorption spectroscopy [39]. As further improvement, the addition of G-nfs also within the compact TiO_2 ($cTiO_2$) layer resulted in reduced device dark-current and improved FF [40], [41].

Moreover, the use of 2-D transition metal carbides, nitrides and carbonitrides (MXenes) has been proposed as an efficient way for tuning the perovskite device energy level alignment [42]. MXenes present a general formula of Mn+1XnTx (n = 1, 2, 3), where M represents an early transition metal, X is a carbon and/or nitrogen atom and Tx, the surface-terminating functional group. By choosing the proper transition metal as well as the relative percentage of T_x terminations (OH, O, F) the easy tuning of MXenes work-function (WF) can be obtained in a large value range (from 1.6 to 6.25 eV) [43]. In particular, when $Ti_3C_2T_x$ MXenes are used as dopant for the perovskite layer, the charge transfer at the perovskite/MXenes interface induces the formation of an interface dipole, causing a reduction of the WF and affecting the band alignment of the entire device. The MXenes incorporation into the perovskite absorber was also demonstrated to passivate the perovskite bulk defects [42], [44] resulting into an improved charge dynamic.

The as realized samples are named G/Mx and their structure is schematically summarized as glass-FTO/$cTiO_2$+G-nfs/$mTiO_2$+G-nfs/perovskite+MXenes/PTAA/MoO_3/ITO [see Fig. 1(c)].

The improved electron dynamic, obtained by engineering the ETL with the addition of G-nfs in both compact and mesoscopic TiO_2 layers, and at the same time the MXenes in the perovskite absorber, reflect in an overall FF enhancement [average increase of 2.2%, see Fig. 5(c)], positively affecting the PCE that results improved up to 27.1%, as reported in Fig. 5(d) and Table IV. These results are justified by an improved electron mobility and electron injection efficiency due to the presence of G-nfs, while the MXenes are responsible for the better band alignment with a consequent improvement of charge transfer from perovskite to ETL and in a reduction of interface losses at both perovskite/CTL interfaces, reflecting in an average J_{SC} improvement [34].

Lastly, we extended our interface engineering approach, by including 2D perovskite layer in the top cell structure, realizing a 3-D/2-D multidimensional perovskite absorbing layer [samples named G/Mx/PEAI, see Fig. 1(d)].

In this regard, the integration of 2-D perovskites into PSCs plays a relevant role as surface passivation layers. More in details, the high conversion efficiency of 3-D perovskites is joined with the superior stability of 2-D perovskites by obtaining a 2-D/3-D vertical bilayer architecture [45], [46], [47], [48].

In this way, the top 2-D perovskite layer can act as surface passivator reducing the surface charge recombination and eventually reflecting in an improved device open circuit voltage (V_{OC}). At the same time, 2-D perovskite acts as a stabilizer layer providing a hydrophobic character to the 3-D perovskite absorber, by ultimately increasing the lifetimes of the PSCs. In

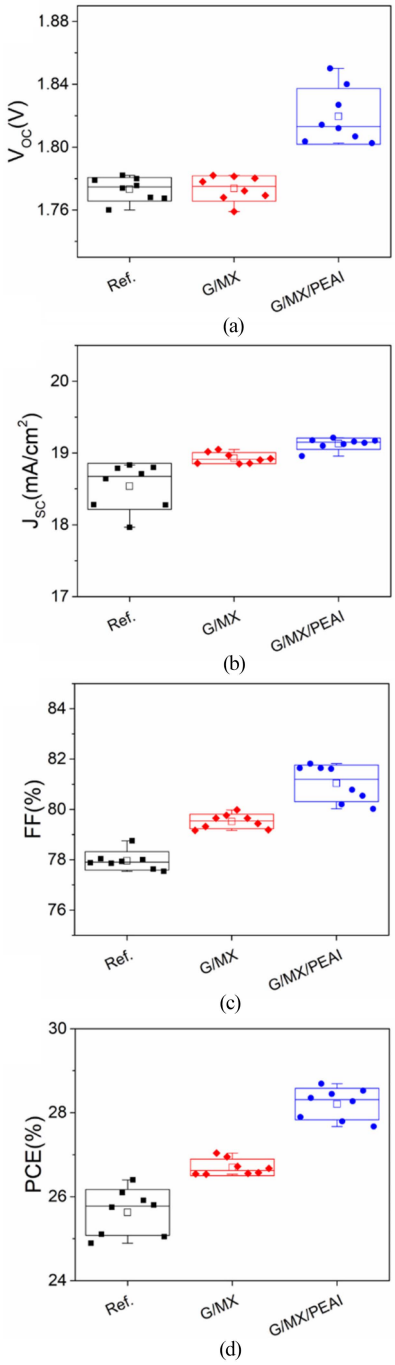

Fig. 5. PV parameters statistics for the investigated tandem solar cells extracted by the I–V characteristics under 1 SUN illumination. (a) V_{OC}. b) J_{SC}. (c) Fill factor. and (d) power conversion efficiency.The statistics were measured on eight samples for each architecture. Cell active area: 0.54 cm^2.

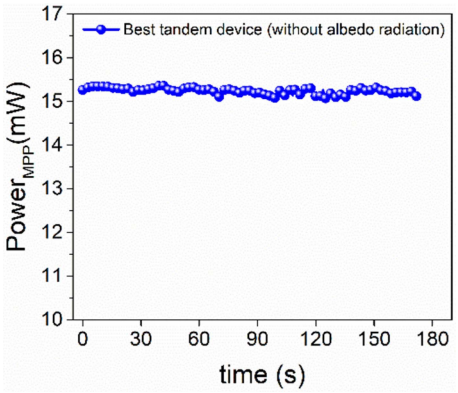

Fig. 6. MPP tracking for the best tandem device employing 2-D materials-engineered perovskite top cell structure (G/MXenes/PEAI).

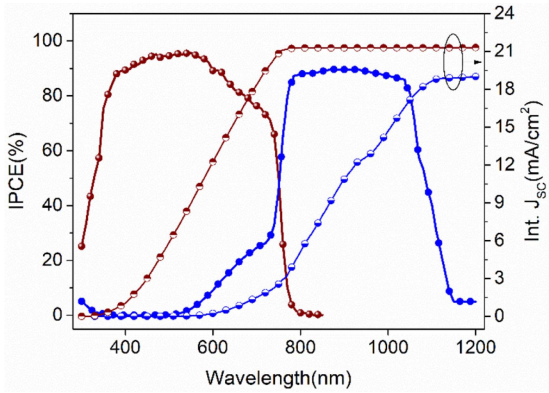

Fig. 7. IPCE spectra for the 2-D material-engineered top perovskite cell (brown circle symbol line) and for the c-Si bottom cell filtered by the perovskite top cell. The integrated currents extraxted by the IPCE spectra are reported in half filled circle symbol lines (brown and blue line for perovskite top and silicon bottom cell respectively).

this article, we realized the layer-by-layer growth by spin coating phenethylammonium iodide (PEAI) on the top mixed halide 3-D perovskite layer. The PbI_2 excess segregated atop the 3-D perovskite, reacting with PEAI, forms a thin layer of 2-D perovskite atop the surface of the 3-D perovskite. In our architecture, the 2-D perovskite lies at the interface with the HTM, causing a reduced interfacial charge carrier recombination, by increasing the device efficiency but also ensuring stable performance under continuous light soaking (1 sun irradiation) with respect to bare 3-D perovskite-based devices.

The resulting 2-D material-engineered perovskite top cell [see the cell structure in Fig. 1(d)] can be resumed as glass-FTO/cTiO$_2$+G-nfs/mTiO$_2$+G-nfs/perovskite+MXenes(MX)/PEAI/PTAA/MoO$_3$/ITO.

Finally, the as-prepared perovskite top cell has been employed in tandem device (namely G/MX/PEAI, schematic reported in Fig. 3) by showing a champion PCE of 28.7% with an overall PCE improvement of about 10.2% with respect to ref. tandem devices [see Fig. 5(d) and Table IV].

The major improvement was observed in both FF and V_{OC} (see Fig. 5). In fact, the surface passivation, produced by 2-D perovskite layer, reduced the surface charge recombination by inducing a remarkable increase in the average V_{OC} (+10.3%) and FF (+3.8%) respectively [see Fig. 5(a) and (c)].

Notably, G/MX/PEAI tandem device exhibited stable performance under prolonged 1 SUN irradiation at maximum power point (MPP), as reported in Fig. 6.

Thanks to the use of 2-D materials within the perovskite top cell structure we were able to boost the tandem device performance above 28.7% (Table IV). The major improvement recorded on J_{SC} was confirmed by the incident power to current conversion efficiency (IPCE) spectrum acquired on the semi-transparent perovskite top cell reported in Fig. 7 .

It is noteworthy that the integrated J_{SC} achieved a final value of 21.5 mA/cm^2 for perovskite top cell, higher than that extracted for the c-Si bottom cell filtered by the perovskite one (integrated $J_{SC} = 19.1$ mA/cm^2). This clearly points out the tandem current is mainly limited by the c-Si bottom cell.

With the aim to overcome such limitation, thanks to the bifaciality the Si HJT cell employed in this article, it is possible to exploit the albedo radiation for filling the current

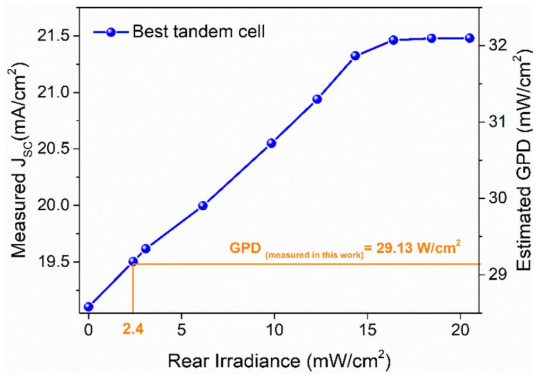

Fig. 8. Measured J_{SC} and estimated GPD for the optimized peorvskite/c-Si tandem cell by varying the albedo irradiance form 0 to 21.5 mW/cm^2. We performed a direct measurement of GDP with a rear irradiance of 2.4 mW/cm^2 obtaining a GDP = 29.13 W/cm^2.

gap between Si and perovskite cells. In particular, we developed an in-house realized sample holder for the *I–V* curve acquisition of 2T mechanically stacked tandem device in presence of the albedo radiation. The albedo radiation was provided through two calibrated white LED, the first one covering the range from 0 to 2.4 mW/cm^2, while the second one up to 24 mW/cm^2. The first LED (LED-1) was fully embeddable in the sample holder used for 1 sun *I–V* measurements, allowing the measuring of the perovskite/c-Si tandem device GPD under sun simulator. On the contrary, the second white LED (LED-2) was embedded in a larger holder, not allowing the retention of the pressure among the constituting sub-cell during all the *I–V* scan, allowing only the J_{SC} to be measured. The range of albedo radiation values considered here is realistic for industrial solar parks optimized to operate with bifacial modules, while rear irradiances as high as 30 mW cm^{-2} may be achieved, in the near future, with the implementation of a reflective coating that covers the ground and through a proper site selection [49].

As suggested in literature, [31] we used the PCE (%) as figure of merit in the case of *I–V* measurements at standard test conditions (STCs, AM1.5G spectrum, 1 sun front-side illumination) and GPD (mW cm^{-2}) for the measurements under

STCs with additional rear irradiance. Notably, when setting a rear irradiation of 2.4 mW/cm^2 with LED-1, the tandem J_{SC} increased up to 19.5 mA/cm^2 in value, recording a final GPD of 29.13 mA/cm^2 under 1 sun front-side irradiation (Table IV). Finally, by linearly changing the albedo radiation using LED-2 we recorded a linear trend for tandem cell J_{SC} till reaching the maximum current generated by the perovskite top cell ($\sim$ 21.5 mA/cm^2 as indicated by the IPCE spectrum reported in Fig. 7) with a sudden saturation thereafter. By roughly retaining the V_{OC} (1.84V) and FF (81.5%) value achieved for the best tandem device, we can estimate a maximum GPD value of about 32 mW/cm^2 (corresponding to a measured tandem J_{SC} of 21.48 mA/cm^2).

This results definitively proofs the use of albedo radiation to reduce the LCOE for perovskite/c-Si tandem devices and paves the way to further explore the concept of bifacial tandem device simply implementing bifacial bottom cell technologies in 2T mechanically stacked architecture.

III. Conclusion

In this article, 2T mechanically stacked perovskite/c-Si tandem cells were realized and optimized in term of PCE. In particular, the use of a PBL atop the PTAA HTL allowed to prevent HTL surface damages during the sputtering of the transparent ITO electrode. Moreover, the optimization of the optoelectronic properties in PSC has been achieved by employing the interface engineering strategy based on specifically selected 2-D materials. While graphene nano-flakes have been employed to dope the PSC photo-electrode (by doping both compact and mesoporous layers), $Ti_3C_2T_x$ MXenes have been used as work function modifier in perovskite absorber while a 2-D PEAI has been deposited atop the 3-D perovskite absorber. The as-engineered perovskite top cell was coupled with a commercially available bifacial c-Si HJT bottom cell without further optimization (produced by EGP) in a 2T mechanically stacked configuration. The as-proposed device structure allowed to easily combine the top and bottom cell separately prepared by simply pressing one cell atop the other, removing the reciprocal fabrication constrains in term of solvent compatibility and applied temperature, occurring when considering the monolithic integration of the composing cells. Top PCE of 28.7% over 0.54 cm^2 active area was achieved under STCs while, thanks to the bifaciality of the c-Si cell employed in this article, an overall GPD of 29.13 mW/cm^2 was demonstrated considering 2.4 mW/cm^2 rear irradiation. The versatility of our approach can be further exploited by easily replacing both perovskite top or c-Si bottom cells with a more performing one. As an example of possible optimization, the rear side silver collecting grids could be further optimized once the c-Si cell is considered for working in tandem configuration in presence of albedo. Indeed, since the maximum generated current is reduced from values around 34 to 22 mA/cm^2, a less dense rear collecting grid could be considered, allowing the reduction of the grid shadowing effect and eventually obtaining the maximum device J_{SC} with lower albedo radiation.

IV. Materials and Methods

PSCs were fabricated on FTO-coated glass substrates (Pilkington, 8 Ω/), which were washed by subsequent sonication steps in acetone, and 2-propanol for 5 and 10 min respectively, in order to remove organic residues from the surface. Silver contacts were screen printed directly over the FTO. These contacts covered and preserved the FTO electrode from the deposition of the subsequent layers. The compact TiO_2 ($cTiO_2$) was deposited by spray pyrolysis at 450 °C starting from a precursor solution of titanium diisopropoxide bis(acetylacetonate), acetylacetone, and ethanol (3:2:45 volume ratio). 10 spray cycles were carried out to achieve a 40-nm-thick layer of $cTiO_2$. The mesoporous TiO_2 ($mTiO_2$) was deposited by spin coating (4000 rpm for 20 s) a Dyesol 30 NRD titania nanoparticle paste diluted with ethanol in a 1:6 mass ratio to obtain 80 nm thick $mTiO_2$ layer. The graphene-doping of both $cTiO_2$ and $mTiO_2$ layers was obtained by mixing the graphene nano-flakes (G-nfs) dispersion in the layer precursor solution (1% in volume). The latter was produced by liquid-phase exfoliation of graphite flakes in N-methyl-2-pyrrolidone and exchanged into ethanol. [39] The graphene-doped TiO_2 solutions were stirred for 2 h before their deposition. The perovskite precursor solution was prepared by weighting PbI_2, FAI, $PbBr_2$, MABr, and CsI in a vial (1:0.81:0.2:0.16:0.06 material molar ratio), followed by the addition of a dimethylformamide (DMF) and dimethyl sulfoxide (DMSO) solvent mixture in 3.16:1 respective proportion. The MXene doping was carried out by adding 0.014 mg of $Ti_3C_2T_x$ MXenes in 1 ml perovskite precursor solution. The deposition of both pristine and MXene-doped perovskite solutions was performed in a N2-filled glove box by spin coating the as-prepared solution with a two-step program at 1000 and 5000 rpm for 10 and 30 s, respectively. A chlorobenzene anti-solvent quenching was performed 7 s before the end of the second spin coating step (realizing a 450 nm thick perovskite overlayer). Subsequently, the samples were annealed for 1 h at 100 °C. A 10 mM solution of 2-phenylethylammonium iodide (PEAI) in 2-propanol was prepared in glovebox and deposited by spin-coater atop the perovskite absorber at 5000 rpm for 30 s. To complete the 2D perovskite layer formation, the samples were annealed at 100 °C for 10 minutes. Poly(triarylamine) (PTAA) solution was prepared by dissolving 10 mg of the material powder in 1 mL of anhydrous toluene. The PTAA solution was deposited onto the perovskite by spin coating at 3300 rpm for 30 s, obtaining a 120 nm thick HTL. Subsequently, 3.5nm of MoO_3 PBL was deposited by mean of high vacuum evaporation technique prior the ITO sputtering deposition. The indium tin oxide (ITO) deposition onto PTAA layers was carried out in a linear magnetron radio frequency (RF) sputtering system (Kenosistek).

Commercial c-Si HJT solar cells were provided by EGP embedding the silver metal grids on both sides. The cell was produced in standard industrial conditions without further modifications. The silicon cell is pressed on the active area of the perovskite cell and the whole stack is kept on a rack that holds the cells together.

Current–voltage (I–V) characteristics of PSCs and perovskite/c-Si tandem devices were acquired in an air

atmosphere by using a solar simulator (ABET Sun 2000, class A) at AM1.5 and 100 mW cm^{-2} illumination conditions, calibrated with a certified reference Si Cell (RERA Solutions RR-1002). Incident power was measured with a Skye SKS 1110 sensor. The class was measured with a BLACKComet Ultraviolet–visible light spectrometer. The devices were not preconditioned before the I–V scan. Both reverse and forward I–V scans were performed by using a scan rate of 50 mV s^{-1}. Any spectral mismatch factor correction was applied to PCE measurements since the class A Abet Sun Simulator employed for the I–V characterization has an error $<1.3\%$ in the spectral region of interest between 300 and 1200 nm, which does not significantly affect the performance measurements accuracy. IPCE measurements were performed through a commercial apparatus (Arkeo all-in-one measurement platform) provided by Cicci Research. The albedo radiation was provided by 2 different white LEDs from Osram (4000K) for the irradiance ranges 0-3 mW/cm^2 and 3-22 mW/cm^2 respectively.

REFERENCES

[1] J. Jeong et al., "Pseudo-halide anion engineering for α-FAPbI3 perovskite solar cells," *Nature*, vol. 592, no. 7854, pp. 381–385, 2021.

[2] C. Liu, Y. Cheng, and Z. Ge, "Chem Soc rev understanding of perovskite crystal growth and film formation in scalable deposition processes," *Chem. Soc. Rev.*, vol. 49, pp. 1653–1687, 2020.

[3] S. Pescetelli et al., "Integration of two-dimensional materials-based perovskite solar panels into a stand-alone solar farm," *Nat. Energy*, vol. 7, pp. 597–607, 2022.

[4] V. Romano, A. Agresti, R. Verduci, and G. D. Angelo, "Advances in perovskites for photovoltaic applications in space," *ACS Energy Lett.*, vol. 7, pp. 2490–2514, 2022.

[5] S. W. Lee, S. Bae, D. Kim, and H. S. Lee, "Historical analysis of high-efficiency, large-area solar cells: Toward upscaling of perovskite solar cells," *Adv. Mater.*, vol. 32, no. 51, 2020, Art. no. 2002202.

[6] Z. Zhang, Z. Li, L. Meng, S. Y. Lien, and P. Gao, "Perovskite-based tandem solar cells: Get the most out of the Sun," *Adv. Function Mater.*, vol. 30, no. 38, 2020, Art. no. 2001904.

[7] T. C. J. Yang, P. Fiala, Q. Jeangros, and C. Ballif, "High-Bandgap perovskite materials for multijunction solar cells," *Joule*, vol. 2, no. 8, pp. 1421–1436, 2018.

[8] A. N. Cho and N. G. Park, "Impact of interfacial layers in perovskite solar cells," *ChemSusChem*, vol. 10, no. 19, pp. 3687–3704, 2017.

[9] A. Fakharuddin, L. Schmidt-Mende, G. Garcia-Belmonte, R. Jose, and I. Mora-Sero, "Interfaces in perovskite solar cells," *Adv. Electron. Mater.*, vol. 7, 2017, Art. no. 1700623.

[10] B. Roose, Q. Wang, and A. Abate, "The role of charge selective contacts in perovskite solar cell stability," *Adv. Energy Mater.*, vol. 9, 2019, Art. no. 1803140.

[11] M. Jošt, L. Kegelmann, L. Korte, and S. Albrecht, "Monolithic perovskite tandem solar cells: A review of the present status and advanced characterization methods toward 30% efficiency," *Adv. Energy Mater.*, vol. 10, no. 26, 2020, Art. no. 1904102.

[12] V. Benda and L. Černá, "PV cells and modules – state of the art, limits and trends," *Heliyon*, vol. 6, no. 12, 2020, Art. no. e05666.

[13] C. O. Ramírez Quiroz et al., "Balancing electrical and optical losses for efficient 4-terminal Si-perovskite solar cells with solution processed percolation electrodes," *J. Mater. Chem. A*, vol. 6, no. 8, pp. 3583–3592, 2018.

[14] B. Chen et al., "Grain engineering for perovskite/silicon monolithic tandem solar cells with efficiency of 25.4%," *Joule*, vol. 3, no. 1, pp. 177–190, 2019.

[15] Accessed: Oct. 1, 2022. [Online]. Available: https://www.nrel.gov/pv/assets/images/efficiency-chart.png

[16] A. Al-Ashouri et al., "Monolithic perovskite/silicon tandem solar cell with $>29\%$ efficiency by enhanced hole extraction," *Science*, vol. 370, no. 6522, pp. 1300–1309, 2020.

[17] L. A. Zafoschnig, S. Nold, and J. C. Goldschmidt, "The race for lowest costs of electricity production: Techno-economic analysis of silicon, perovskite and tandem solar cells," *IEEE J. Photovolt.*, vol. 10, no. 6, pp. 1632–1641, Nov. 2020.

[18] C. Battaglia, A. Cuevas, and S. De Wolf, "High-efficiency crystalline silicon solar cells: Status and perspectives," *Energy Environ. Sci.*, vol. 9, no. 5, pp. 1552–1576, 2016.

[19] Y. Hou et al., "Efficient tandem solar cells with solution-processed perovskite on textured crystalline silicon," *Science*, vol. 367, no. 6482, pp. 1135–1140, 2020.

[20] B. Chen et al., "Blade-coated perovskites on textured silicon for 26%-efficient monolithic perovskite/silicon tandem solar cells," *Joule*, vol. 4, no. 4, pp. 850–864, 2020.

[21] A. S. Subbiah et al., "High-performance perovskite single-junction and textured perovskite/silicon tandem solar cells via slot-die-coating," *ACS Energy Lett.,* vol. 5, no. 9, pp. 3034–3040, 2020.

[22] E. Lamanna et al., "Mechanically stacked, two-terminal graphene-based perovskite /silicon tandem solar cell with efficiency over 26%," *Joule*, vol. 4, pp. 865–881, 2020.

[23] M. De Bastiani et al., "Recombination junctions for efficient monolithic perovskite-based tandem solar cells: Physical principles, properties, processing and prospects," *Mater. Horiz.*, vol. 7, no. 11, pp. 2791–2809, 2020.

[24] S. P. Bremner, M. Y. Levy, and C. B. Honsberg, "Analysis of tandem solar cell efficiencies under AM1.5G spectrum using a rapid flux calculation method," *Prog. Photovolt. Res. Appl.*, vol. 16, pp. 225–233, 2008.

[25] N. Rolston et al., "Engineering stress in perovskite solar cells to improve stability," *Adv. Energy Mater.*, vol. 8, no. 29, 2018, Art. no. 1802139.

[26] N. Rolston et al., "Mechanical integrity of solution-processed perovskite solar cells," *Extreme Mech. Lett.*, vol. 9, pp. 353–358, 2016.

[27] I. L. Braly et al., "Current-induced phase segregation in mixed halide hybrid perovskites and its impact on two-terminal tandem solar cell design," *ACS Energy Lett.*, vol. 2, no. 8, pp. 1841–1847, 2017.

[28] A. Onno et al., "Predicted power output of silicon-based bifacial tandem photovoltaic systems," *Joule*, vol. 4, no. 3, pp. 580–596, 2020.

[29] K. Jäger, P. Tillmann, E. A. Katz, and C. Becker, "Perovskite/silicon tandem solar cells: Effect of luminescent coupling and bifaciality," *Sol. RRL*, vol. 5, no. 3, 2021, Art. no. 2000628.

[30] M. De Bastiani et al., "Efficient bifacial monolithic perovskite/silicon tandem solar cells via bandgap engineering," *Nat. Energy*, vol. 6, no. 2, pp. 167–175, 2021.

[31] S. Bellani et al., "Solution-processed two-dimensional materials for next-generation photovoltaics," *Chem. Soc. Rev.*, vol. 50, no. 21, pp. 11870–11965, 2021.

[32] H. Kanda et al., "Analysis of sputtering damage on I-V curves for perovskite solar cells and simulation with reversed diode model," *J. Phys. Chem. C*, vol. 120, no. 50, pp. 28441–28447, 2016.

[33] N. Ahn et al., "Trapped charge-driven degradation of perovskite solar cells," *Nat. Commun.*, vol. 7, no. 1, pp. 1–9, 2016.

[34] S. Pescetelli et al., "Synergic use of two-dimensional materials to tailor interfaces in large area perovskite modules," *Nano Energy*, vol. 95, May 2022, Art. no. 107019.

[35] A. Di Carlo, A. Agresti, F. Brunetti, and S. Pescetelli, "Two-dimensional materials in perovskite solar cells," *J. Phys. Energy*, vol. 2, 2020, Art. no. 031003.

[36] R. Verduci, A. Agresti, V. Romano, and G. D'angelo, "Interface engineering for perovskite solar cells based on 2d-materials: A physics point of view," *Materials*, vol. 14, no. 19, 2021, Art. no. 5843.

[37] F. Biccari et al., "Graphene-based electron transport layers in perovskite solar cells: A step-up for an efficient carrier collection," *Adv. Energy Mater.*, vol. 7, no. 22, 2017, Art. no. 1701349.

[38] Y. Busby et al., "Aging effects in interface-engineered perovskite solar cells with 2D nanomaterials: A depth profile analysis," *Mater. Today Energy*, vol. 9, pp. 1–10, 2018.

[39] P. O'Keeffe et al., "Graphene-induced improvements of perovskite solar cell stability: Effects on hot-carriers," *Nano Lett.*, vol. 19, no. 2, pp. 684–691, 2019.

[40] A. Agresti et al., "Graphene and related 2D materials for high efficient and stable perovskite solar cells," in *Proc. 17th IEEE Int. Conf. Nanotechnol.*, 2017, pp. 145–150.

[41] S. Razza, S. Pescetelli, A. Agresti, and A. Di Carlo, "Laser processing optimization for large-area perovskite solar modules," *Energies*, vol. 14, 2021.

[42] A. Agresti et al., "Titanium-carbide MXenes for work function and interface engineering in perovskite solar cells," *Nat. Mater.*, vol. 18, pp. 1228–1234, 2019.

[43] T. Schultz et al., "Surface termination dependent work function and electronic properties of Ti3C2Tx MXene," *Chem. Mater.*, vol. 31, no. 17, pp. 6590–6597, 2019.
[44] D. Saranin et al., "Transition metal carbides (MXenes) for efficient NiO-based inverted perovskite solar cells," *Nano Energy*, vol. 82, 2021, Art. no. 105771.
[45] S. Pescetelli, A. Agresti, S. Razza, L. A. Castriotta, and A. Di Carlo, "Large area perovskite solar modules with improved efficiency and stability," in *Proc. Int. Symp. Adv. Electron. Commun. Technol.*, 2019, pp. 1–5.
[46] B. Hailegnaw et al., "Optoelectronic properties of layered perovskite solar cells," *Sol. RRL*, vol. 3, no. 8, 2019, Art. no. 1900126.
[47] L. Zhou et al., "Highly efficient and stable planar perovskite solar cells with modulated diffusion passivation toward high power conversion efficiency and ultrahigh fill factor," *Sol. RRL*, vol. 3, no. 11, 2019, Art. no. 1900293.
[48] M. Degani et al., "23.7% Efficient inverted perovskite solar cells by dual interfacial modification," *Sci. Adv.*, vol. 7, no. 49, 2021, Art. no. eabj7930.
[49] H. Liu, et al., "Worldwide theoretical comparison of outdoor potential for various silicon-based tandem module architectures," in *Proc. IEEE Conf. Rec. Photovolt. Specialists Conf.*, 2021, pp. 377–381.